Cell Chemical Biology
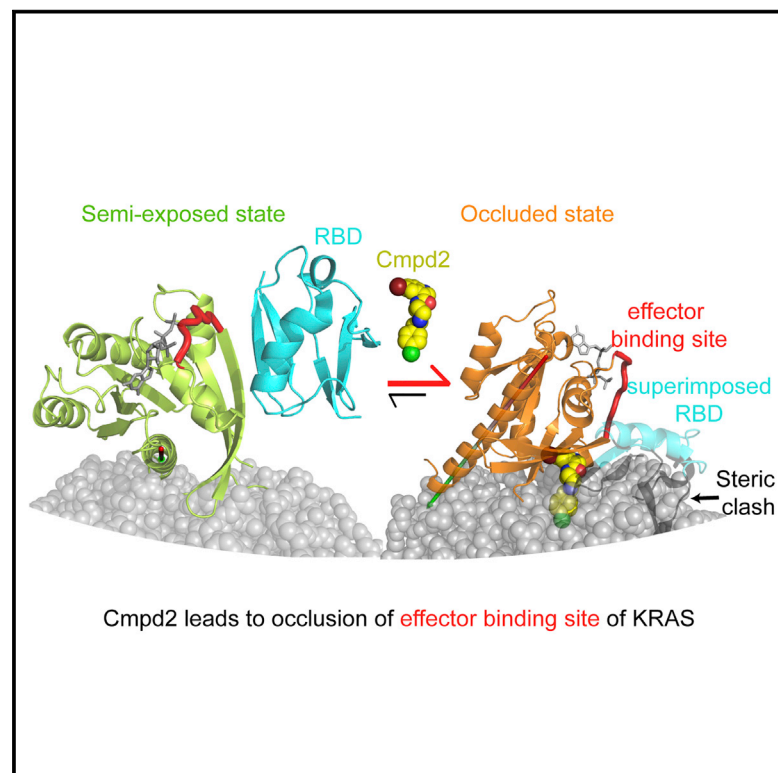
Inhibition of K-RAS4B by a Unique Mechanism of Action: Stabilizing Membrane-Dependent Occlusion of the Effector-Binding Site

Graphical Abstract

Cmpd2 leads to occlusion of effector binding site of KRAS

Highlights

- Mechanism of membrane-dependent inhibition of prenylated KRAS by Cmpd2 was elucidated

- Cmpd2 simultaneously engages KRAS and the membrane surface

- Cmpd2 stabilizes a KRAS orientation where membrane occludes its effector-binding site

- Partitioning of Cmpd2 to the membrane enhances its potency

Authors

Zhenhao Fang,
Christopher B. Marshall,
Tadateru Nishikawa, Alvar D. Gossert,
Johanna M. Jansen, Wolfgang Jahnke,
Mitsuhiko Ikura

Correspondence

cmarshal@uhnresearch.ca (C.B.M.),
mikura@uhnresearch.ca (M.I.)

In Brief

Fang et al. have elucidated a membrane-dependent mechanism by which a small-molecule inhibitor of KRAS binds at the protein-membrane interface and stabilizes KRAS in an orientation in which its effector-binding site is occluded by the membrane.

CellPress

Inhibition of K-RAS4B by a Unique Mechanism of Action: Stabilizing Membrane-Dependent Occlusion of the Effector-Binding Site

Zhenhao Fang,[1] Christopher B. Marshall,[1,*] Tadateru Nishikawa,[1] Alvar D. Gossert,[3,4] Johanna M. Jansen,[2] Wolfgang Jahnke,[3] and Mitsuhiko Ikura[1,5,*]

[1]Department of Medical Biophysics, University of Toronto, Princess Margaret Cancer Centre, University Health Network, Toronto, ON M5G 2M9, Canada
[2]Department of Global Discovery Chemistry, Novartis Institutes for BioMedical Research, Emeryville, CA 94608, USA
[3]Chemical Biology and Therapeutics, Novartis Institutes for BioMedical Research, Basel 4002, Switzerland
[4]Institute for Molecular Biology and Biophysics, Department of Biology, ETH Zürich, Zürich 8093, Switzerland
[5]Lead Contact
*Correspondence: cmarshal@uhnresearch.ca (C.B.M.), mikura@uhnresearch.ca (M.I.)
https://doi.org/10.1016/j.chembiol.2018.07.009

SUMMARY

KRAS is frequently mutated in several of the most lethal types of cancer; however, the KRAS protein has proven a challenging drug target. K-RAS4B must be localized to the plasma membrane by pre-nylation to activate oncogenic signaling, thus we endeavored to target the protein-membrane interface with small-molecule compounds. While all reported lead compounds have low affinity for KRAS in solution, the potency of Cmpd2 was strongly enhanced when prenylated K-RAS4B is associated with a lipid bilayer. We have elucidated a unique mechanism of action of Cmpd2, which simultaneously engages a shallow pocket on KRAS and associates with the lipid bilayer, thereby stabilizing KRAS in an orientation in which the membrane occludes its effector-binding site, reducing RAF binding and impairing activation of RAF. Furthermore, enrichment of Cmpd2 on the bilayer enhances potency by promoting interaction with KRAS. This insight reveals a novel approach to developing inhibitors of membrane-associated proteins.

INTRODUCTION

For more than three decades, mutations that hyper-activate RAS proteins have been recognized as drivers of multiple cancer types. Among the RAS isoforms, K-RAS is the most frequently mutated in human cancers, as it is altered in ~22% of all tumors, and most prevalent in pancreatic, colon, and lung cancers (Prior et al., 2012). K-RAS4B, the predominant K-RAS splice variant expressed in human tissues, comprises a GTPase domain followed by a polybasic region (PBR) and a C-terminal CaaX-box that specifies farnesylation of Cys-185. The PBR and farnesyl group localize K-RAS4B to

the plasma membrane, which is required for RAS signaling output. The oncogenicity of K-RAS spurred a long-standing interest in targeting this protein, which proved challenging due to a lack of classical "druggable pockets"; however, recent reports of new lead compounds have reinvigorated these efforts (Cox et al., 2014; Spiegel et al., 2014; Stephen et al., 2014). Using an assay to screen for inhibitors of BRAF activation by the prenylated form of the oncogenic K-RAS4B G12V mutant in the presence of phosphatidylserine (PS), a lead compound with a half maximal inhibitory concentration (IC_{50}) <1 μM *in vitro* and half maximal effective concentration (EC_{50}) <5 μM in cells was discovered (Jansen et al., 2017). This compound (Cmpd2) is composed of piperidine, chloro-benzyl, and indole fragments. Bio-layer interferometry (BLI) experiments demonstrated that the affinity (K_d < 1 μM) of Cmpd2 for prenylated K-RAS4B in the presence of PS is consistent with its potency. Interestingly, the affinity of Cmpd2 for the truncated, soluble GTPase domain of K-RAS determined by nuclear magnetic resonance (NMR) was much weaker (K_d = 700 μM), suggesting that the lipids play a role in increasing the affinity of Cmpd2 for K-RAS4B. Here we investigate the mechanism underlying the lipid bilayer-dependent enhancement of the affinity of Cmpd2 for preny-lated K-RAS4B.

Although crystal structures of K-RAS in complex with several low-affinity and covalent lead compounds have now been solved (Cox et al., 2014; Ostrem and Shokat, 2016), there is little structural information available about how these inhibitors may affect interactions between K-RAS4B and the lipid bilayer. We previously utilized NMR spectroscopy to derive atomic-scale structural models of the dynamic interactions between K-RAS4B and lipid bilayers using nanodiscs (Mazhab-Jafari et al., 2015), which are 5 × 10-nm discoidal lipid bilayers bound and stabilized by a membrane scaffold protein (Denisov et al., 2004; Schuler et al., 2013). Here we have applied this high-resolution NMR approach to charac-terize a ternary interaction between K-RAS4B, Cmpd2, and a lipid bilayer containing 20% PS. Our results strongly argue that Cmpd2 stabilizes a conformational state and the orientation of K-RAS4B in which the effector-binding
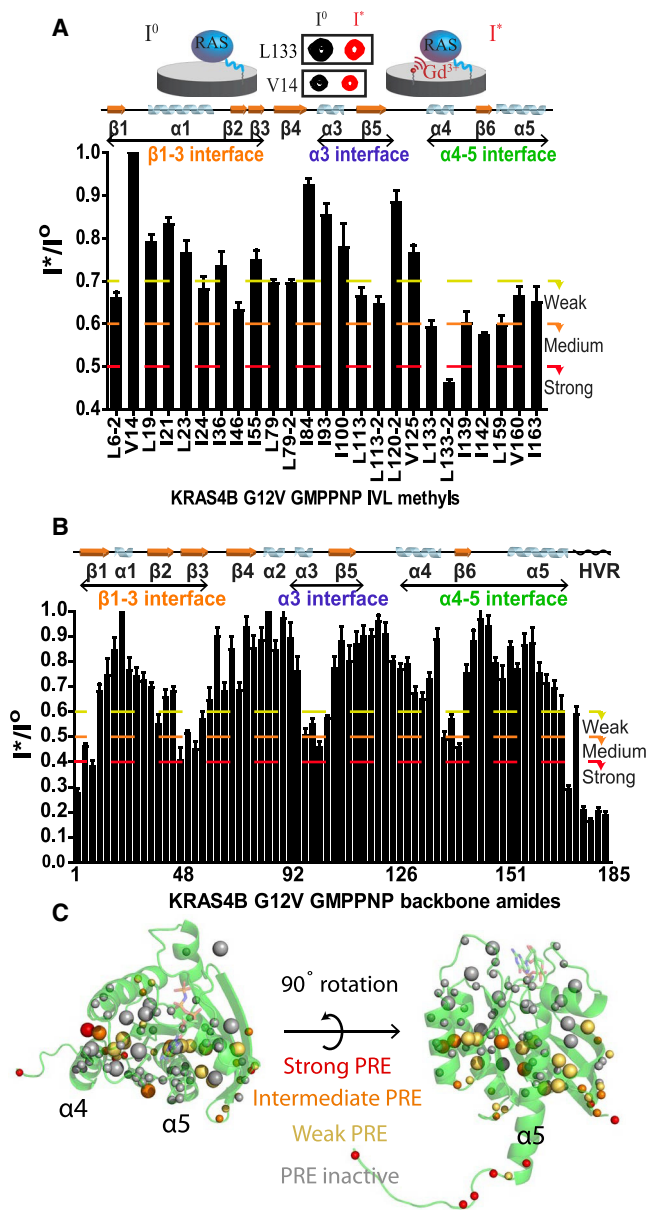
Figure 1. Mapping the Membrane-Association Interface on K-RAS4B G12V

(A and B) Paramagnetic relaxation enhancement (PRE) induced by Gd^{3+} chelated on the lipid bilayer surface on Ile-$C\delta$, Val-$C\gamma$, and Leu-$C\delta$ resonances (A) and backbone amide resonances (B) of GMPPNP-bound K-RAS4B G12V. I^*/I^o is the ratio of peak heights in the presence/absence of Gd^{3+}, and error bars represent spectral noise.

(C) Distribution of PRE-insensitive (gray), weak (yellow), intermediate (orange), and strong (red) PRE probes—as defined by thresholds in (A and B)—mapped on the K-RAS4B structure (PDB: 4DST). Large and small spheres represent methyls and amides, respectively.

See also Figures S1 and S2 and Table S1.

site is occluded at the membrane interface. This inhibits signaling output by making RAF binding less favorable and interfering with the process by which KRAS activates RAF.

RESULTS AND DISCUSSION

Expanded NMR Probe Set Revealed More Comprehensive Analysis of K-RAS4B-Membrane Interface

To study K-RAS interactions with the membrane by NMR, a K-RAS4B G12V (residues 1–185) construct bound to the GTP analog GMPPNP was used. This protein was prepared with uniform ^{15}N labeling (Figure S1B) and selective ^{13}C labeling of Ile Cδ (11 residues), Val Cγ (3), and Leu Cδ (11) methyls. In the ^{15}N TROSY spectrum ~125 peaks were observed, due to broadening of peaks in the dynamic switch regions, and 82 well-resolved peaks could be assigned by directly transferring assignments from Biological Magnetic Resonance Bank entry 17785 (KRAS GMPPNP) as well as our KRAS PBR assignment.

The protein was tethered to a lipid bilayer by covalently cross-linking Cys185 to maleimide-functionalized phosphoethanol-amine preassembled in nanodiscs comprised of DOPC/DOPS (4:1) (Figure S1A). Compared with free K-RAS4B, tethering K-RAS4B to nanodiscs broadened the line-width of resonances from the G-domain while sharpening several signals from the PBR (Figure S1C). We further incorporated a lipid with the para-magnetic ion gadolinium (Gd^{3+}) chelated by DTPA on the head group, as we described previously (Mazhab-Jafari et al., 2015), to identify K-RAS4B residues proximal to the bilayer surface by resonances broadened due to paramagnetic relaxation enhancement (PRE) (Figures 1A and S1D). All of the methyl peaks and 72 of the 82 assigned amide peaks exhibited sufficient signal to noise for analysis of PRE. The PRE effects were most prominent on three surfaces of K-RAS4B G12V, comprising helices $\alpha3$-4, $\alpha4$-5 and strands $\beta1$-3 (Figure 1). The $\alpha4$-5 and $\beta1$-3 interfaces were identified in our previous study of K-RAS4B G12D using 11 ^{13}C Ile Cδ probes; however, detection of the $\alpha3$-4 interface, which was predicted in a recent molecular dynamics simulation (Prakash et al., 2016), required the addition of ^{13}C-Leu/Val and ^{15}N-amide probes, because it lacks surface-exposed Ile. The ^{13}C and ^{15}N probes were categorized according to the magnitude of PRE-induced peak broadening (Figures 1A and 1B), and those exhibiting strong, moderate, or weak PRE were mapped on the K-RAS4B structure (Figure 1C), together with "PRE-insensitive" probes that were broadened by <30% (^{13}C) or <40% (^{15}N). The PRE-sensitive probes cluster where the three interfaces described above converge near the PBR (Figure 1C, left), which tethers K-RAS4B to the membrane and therefore experiences strong PRE (Figures 1B and 1C). The probes that exhibit intermediate and strong PRE were used as distance restraints in high ambiguity-driven biomolecular docking (HADDOCK) simulations to build structural models of K-RAS4B on the bilayer (Table S1, left panel). Among the final 200 HADDOCK docking solutions, K-RAS4B was observed in five distinct clusters including an "occluded" orientation (O_1) in which K-RAS4B contacts the membrane through $\beta1$-3, whereby the effector-binding site (switch I) is occluded by the membrane surface (Figures 2A and 2B). In the largest cluster (E_1), $\alpha4$-5 contacts the membrane and switch I is exposed, while two additional small clusters comprise a continuum of exposed orientations (E_2 and E_3) involving the adjacent faces $\alpha4$ and $\alpha3$-4, and the final cluster comprises a semi-exposed (SE) orientation mediated by $\alpha5$ (Figures 2A and 2B).
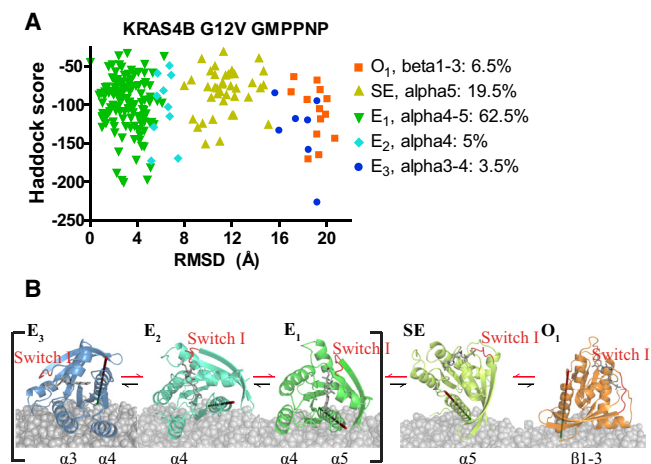
Figure 2. HADDOCK-Derived Models of K-RAS4B Orientations on a Lipid Bilayer

(A) Cluster analysis of 200 PRE-driven HADDOCK models of the K-RAS4B-nanodisc complex, represented on a plot of HADDOCK score versus root-mean-square deviation (RMSD) to the mean structure in the E_1 cluster defined as the structure in E_1 with lowest RMSD to all other 199 structures, calculated as described in Mazhab-Jafari et al. (2015). Populations of individual clusters are given as percentages.

(B) PRE-based models of the K-RAS4B-nanodisc complex derived from five K-RAS4B orientation clusters: exposed (E_1/E_2/E_3), semi-exposed (SE), and occluded (O_1). Secondary structural elements involved in membrane contacts are annotated, and an arrow is drawn through the axis of helix 5 (N-terminal, red, to C-terminal, green) to convey orientation.

See also Figure S6 and Table S2.

Cmpd2 Stabilized the Occluded Orientation of K-RAS4B on the Membrane

Using the PRE on Ile36 as an indicator, we previously found that the population of the K-RAS4B occluded state is decreased by the highest frequency oncogenic mutation G12D (Mazhab-Jafari et al., 2015). Here we show that the second most frequent mutation, G12V, exerts a similar effect (Figures 3A and 3B), indicating that reorientation of K-RAS4B is not a direct electrostatic effect of an anionic substitution. To determine how K-RAS4B orientation impacts effector-binding affinity, we compared the affinity for BRAF-RAS-binding domain (RBD) of nanodisc-associated K-RAS4B wild-type (WT) versus G12V (Figure S2D). We and others previously showed that in solution the G12V mutation reduces the affinity for RAF RBDs by severalfold (Hunter et al., 2015; Smith and Ikura, 2014), whereas here we found that when K-RAS4B is tethered to a bilayer, the G12V mutation is less disruptive (affinity is ~30% lower than WT), likely because the increase in the exposed state partially offsets the reduction in inherent affinity. Since inhibition of K-RAS4B G12V by Cmpd2 was potentiated by the presence of lipids, we examined whether Cmpd2 affects the orientation of K-RAS4B G12V GMPPNP on a bilayer. Analyzing the PRE effect on Ile36 in a first step, we found that addition of Cmpd2 remarkably increased the population of the occluded conformation, as seen by a significant increase in the PRE effect on Ile36, as well as Ile55 (near the binding site as defined below) (Figure 3C). We also examined the effect of Cmpd2 on K-RAS4B WT, which exhibits a larger population of occluded orientation than G12V as detected by
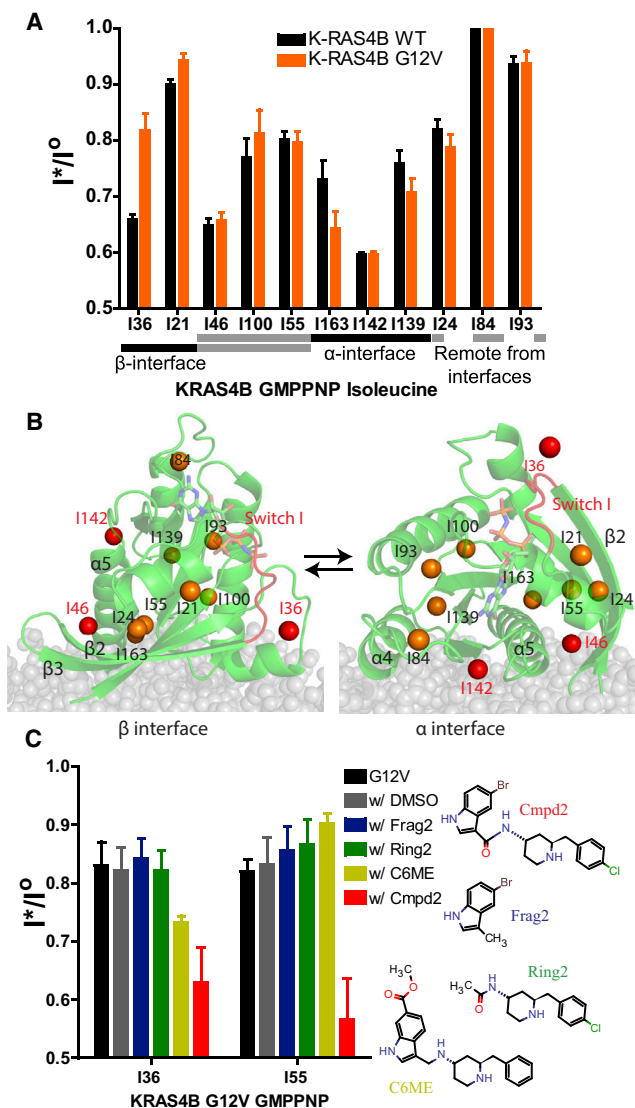

Figure 3. Cmpd2 Reverses the K-RAS4B Exposed Orientation Shift on the Lipid Bilayer Induced by the Oncogenic Mutation G12V

(A) PRE broadening of ^{13}C Ile Cδ resonances of nanodisc-tethered GMPPNP-bound K-RAS4B WT (black) versus G12V mutant (red) by Gd^{3+} chelated by PE-DTPA.

(B) Distribution of K-RAS4B Ile-Cδ probes on K-RAS4B structure (red, broadened >30% in WT; orange, broadened <30% in WT). A similar analysis of K-RAS4B G12V is presented in Figure 1C. Position of Ile-Cδ probes relative to the membrane surface of E_1 (left) and O_1 (right) orientation is highlighted.

(C) PRE effect on Ile36 and Ile55-Cδ of nanodisc-tethered K-RAS4B G12V GMPPNP in the absence and presence of compounds including Cmpd2, Ring2, Frag2, and C6ME. Chemical structure of compounds shown at right. Error bars in (A and C) represent spectral noise.

See also Figures S2 and S4 and Table S5.

the PRE of Ile36 (Figure S2E). Addition of Cmpd2 further increased the PRE on Ile36 of K-RAS4B WT, but the change was smaller than that of G12V, indicating that Cmpd2 may be more active against the mutant that was originally screened (Jansen et al., 2017). The indole fragment of Cmpd2 (Frag2, Figure 3C) resembles lead compounds previously reported to bind
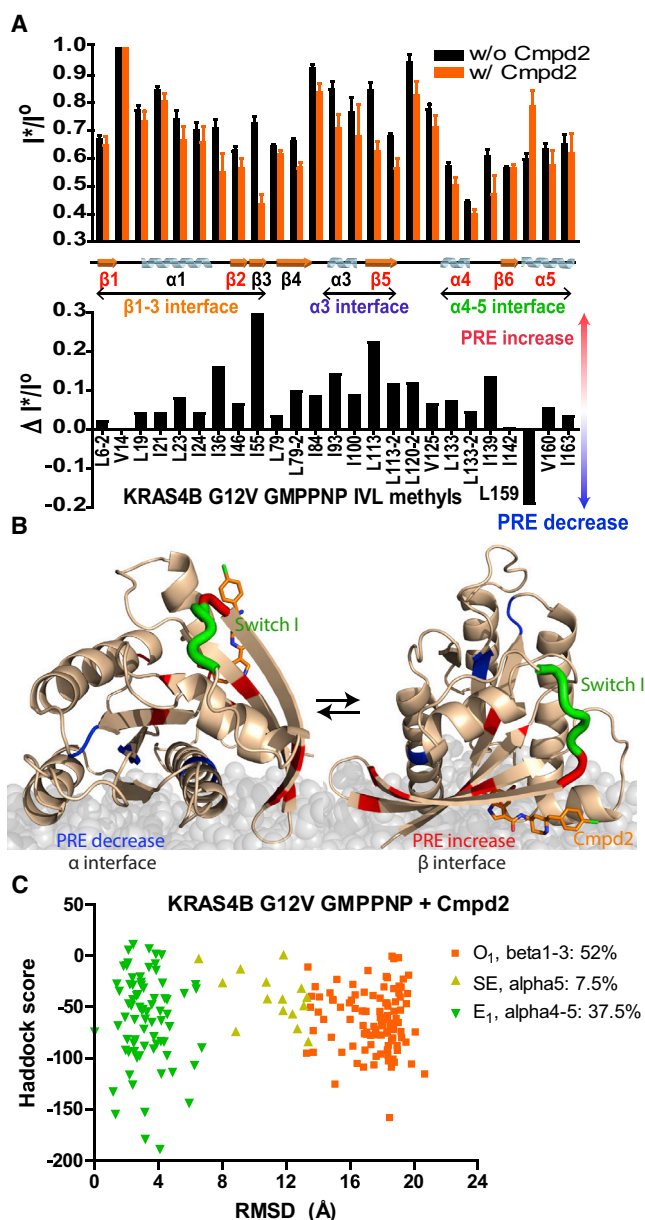
Figure 4. Cmpd2 Shifts K-RAS4B G12V Orientation Equilibrium from Exposed State to Occluded State

(A) PRE induced by Gd^{3+} chelated on the lipid bilayer surface on Ile-Cδ, Val-Cγ, and Leu-Cδ resonances of GMPPNP-bound K-RAS4B G12V in absence (black) and presence (red) of 1 mM Cmpd2. Lower panel: change in PRE effect upon addition of Cmpd2. Error bars represent spectral noise.

(B) K-RAS4B residues that exhibit increased (red) or decreased (blue) PRE in the presence of Cmpd2 are mapped on the ribbon structure, together with the Cmpd-2 binding site (Cmpd2 is shown in orange). The position of the membrane surface in the E_1 (gray) and O_1 (purple) orientations is highlighted.

(C) Cluster analysis of 200 PRE-driven HADDOCK models of the K-RAS4B-nanodisc-Cmpd2 complex, represented on a plot of HADDOCK score versus RMSD to the mean structure in the E_1 cluster. The O_1 cluster is populated to 52% in the presence of Cmpd2 versus 6.5% in absence of Cmpd2.

See also Figures S2 and S7, and Tables S1, S3, and S4.

to K-RAS4B (Maurer et al., 2012; Sun et al., 2012), and was found to be sufficient for binding to K-RAS4B in solution with low affinity (Figure S3A). However, neither Frag2 nor the piperidine-chlorobenzyl fragment (Ring2) alone was sufficient to affect the orientation of K-RAS4B G12V on the membrane, indicating that this function requires a linkage between both fragments (Figure 3C). To investigate the importance of the interaction of Cmpd2 with K-RAS4B on the orientation of the protein, we used a similar compound (C6ME), with a piperidine-benzyl fragment linked to an indole lacking the C5-Br and bearing a C6-methyl ester, which disrupts binding to unprocessed K-RAS4B G12V (Figure S3B), and shows only weak inhibition of RAS-mediated RAF activation (Table S5). As expected, C6ME did not affect PRE near the Cmpd2 binding site (Ile55). Surprisingly, C6ME did modulate the PRE on some residues, including a modest increase on Ile36, suggesting that, in addition to specific interactions between Cmpd2 and K-RAS4B (described below), this family of indole-piperidine-benzyl compounds may further impact K-RAS4B interactions with the membrane through non-specific perturbations of the lipid bilayer. The effects of this series of compounds on K-RAS4B orientation (Figure 3C) correlate with inhibition of K-RAS4B-mediated activation of RAF in the coupled assay (Table S5), in which Frag2, C6ME, and Cmpd2 exhibited progressively increasing inhibitory effects (Table S5). The methyl ester of C6ME impairs binding to the KRAS indole pocket, and thereby reduces its impact on the conformational equilibrium as well as inhibition of RAF activation.

To derive a more comprehensive understanding of the mechanism by which Cmpd2 changes K-RAS4B orientation, we analyzed the effect of Cmpd2 on the PRE of all the ^{13}C and ^{15}N probes described above. The increased total number (99) of the NMR probes relative to our previous studies using 11 ^{13}C Ile Cδ probes (Mazhab-Jafari et al., 2015) was the key to dissect the effect of Cmpd2 on K-RAS4B conformation on the membrane. The addition of Cmpd2 increased PRE-induced global line broadening on most of the ^{13}C methyl (Figure 4A) and ^{15}N amide probes (Figure S2B) of nanodisc-tethered K-RAS4B, indicating that it stabilized interactions between K-RAS4B and the bilayer surface, which was not observed with C6ME. The few probes that exhibited significantly reduced PRE with addition of Cmpd2 are located in α5 and β5 (Figures 4A and S2B), indicating a decrease in the major exposed orientation E_1. Those showing more PRE in the presence of Cmpd2 cluster around the β interface of K-RAS4B G12V (Figure 4B), which coincides with the Cmpd2-binding site mapped by chemical shift perturbations (CSPs) (Figures S3C and S3D) and nuclear Overhauser effects (NOEs) (Figure S4A; Table S6). The addition of Cmpd2 to either the GDP- or GMPPNP-bound forms of K-RAS4B G12V (1–185) in solution induced CSPs in the ^1H-^{15}N heteronuclear single quantum coherence (HSQC) spectrum, which mapped to two regions, one close to L56 and the other near H95 (Figures S3C and S3D). NOE restraints between Cmpd2 indole protons and residues V7, L56, T58, M72, and T74 of KRAS-GDP in solution (Jansen et al., 2017) (Table S6) unambiguously mapped the binding site to a pocket adjacent to switch I that overlaps with the binding site previously identified by crystallography for two similar indole derivatives, Cmpd13 and DCAI (Maurer et al., 2012; Sun et al., 2012) (Figure S4). These other indoles also
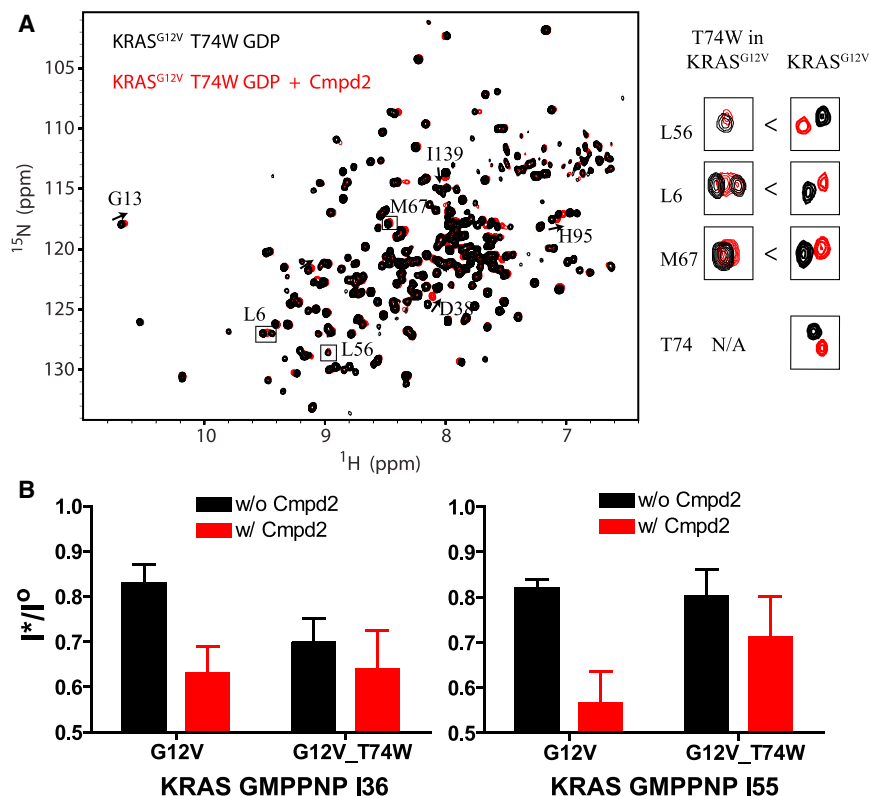
A

KRAS^G12V T74W GDP

KRAS^G12V T74W GDP + Cmpd2

B

spectrum (Figure 5). In solution, the T74W mutant exhibited fewer and smaller CSPs on key residues near the main binding pocket upon addition of Cmpd2 (Figure 5A), demonstrating that the mutation reduced binding as expected. When tethered to nanodiscs, the T74W mutation diminished the Cmpd2-induced enhancement of PRE on the β interface of K-RAS4B^G12V (Figure 5B), thus supporting a requirement for specific interaction of Cmpd2 with K-RAS4B to stabilize the occluded orientation.

perturbed the H95 region on α3 (Maurer et al., 2012; Sun et al., 2012), suggesting an allosteric connection to the switch I binding pocket, although we cannot rule out the possibility that this site may exhibit weak affinity for the indoles. Using NOE-based distance restraints, we carried out HADDOCK simulations to build structural models of Cmpd2 bound to K-RAS4B in solution. With a rich network of intermolecular NOE restraints between the indole fragment of Cmpd2 and 8 residues, it is invariably found in the binding pocket formed by K5 and V7 on β1 and L56 and T58 on β3 in the ensemble of models, while the piperidine-chlorobenzyl fragment can be observed in a position between switch I and α2 in the major cluster, where it forms hydrophobic interactions with M67 (Figure S4A). The indole-binding pocket is not present in most RAS crystal structures; however, a similar pocket was observed in a structure of H-RAS-GMPPNP in an alternate, signaling-incompetent conformation designated "state I" (PDB: 4EFM; Muraoka et al., 2012). Interestingly, Cmpd2 stabilizes state I of K-RAS4B G12V (Jansen et al., 2017), suggesting conformational selection as a mode of binding.

To confirm that the shift toward the occluded orientation induced by Cmpd2 depends upon specific binding to K-RAS4B, a mutation (T74W) was introduced to the Cmpd2-binding pocket to disrupt binding of the compound. T74 is not highly conserved in the RAS subfamily, and we predicted that the introduction of a Trp side chain would partially occupy the Cmpd2-binding site. Further, some RAS subfamily members have Trp in this position, suggesting that the substitution would be unlikely to disrupt folding, which was confirmed by the HSQC

Cmpd2 Simultaneously Engaged the K-RAS4B β Interface and the Surface of the Lipid Bilayer

The Cmpd2 binding site is located on the β interface of K-RAS4B, and the increased PRE on this region indicates that its proximity to the bilayer is enhanced by addition of Cmpd2 (Figure 4B). This suggests that Cmpd2 simultaneously engages both the K-RAS4B β interface and the surface of the bilayer, acting as a "glue" that stabilizes this occluded orientation. To investigate interactions between Cmpd2 and the lipid bilayer, we analyzed the NMR spectra of the compound in the presence or absence of nanodiscs and/or K-RAS4B (Figure S5). K-RAS4B alone perturbed the chemical shifts of indole-ring protons (H2, H3, and H6, Figure S5B), consistent with the observed NOEs. In the presence of 20% DOPS nanodiscs, the sharp ^1H resonances of Cmpd2 were all severely broadened and the chemical shifts exhibited large perturbations (Figure S5B), indicating a strong interaction between Cmpd2 and the nanodiscs, consistent with its calculated LogP (cLogP) value of 4.4 (Figure 6A). To discriminate which part of Cmpd2 contributes to K-RAS4B and nanodisc binding, the bromo-indole (Frag2) and piperidine-chlorobenzyl (Ring2) fragments were studied separately. In isolation, Frag2 peaks were strongly perturbed by nanodiscs, whereas Ring2 peaks were severely broadened (Figures S5C and S5D), suggesting that both the indole (cLogP 3.3) and piperidine-chlorobenzyl (cLogP 2.6) rings contribute to the association with lipids. The characteristic surface trimethylamine
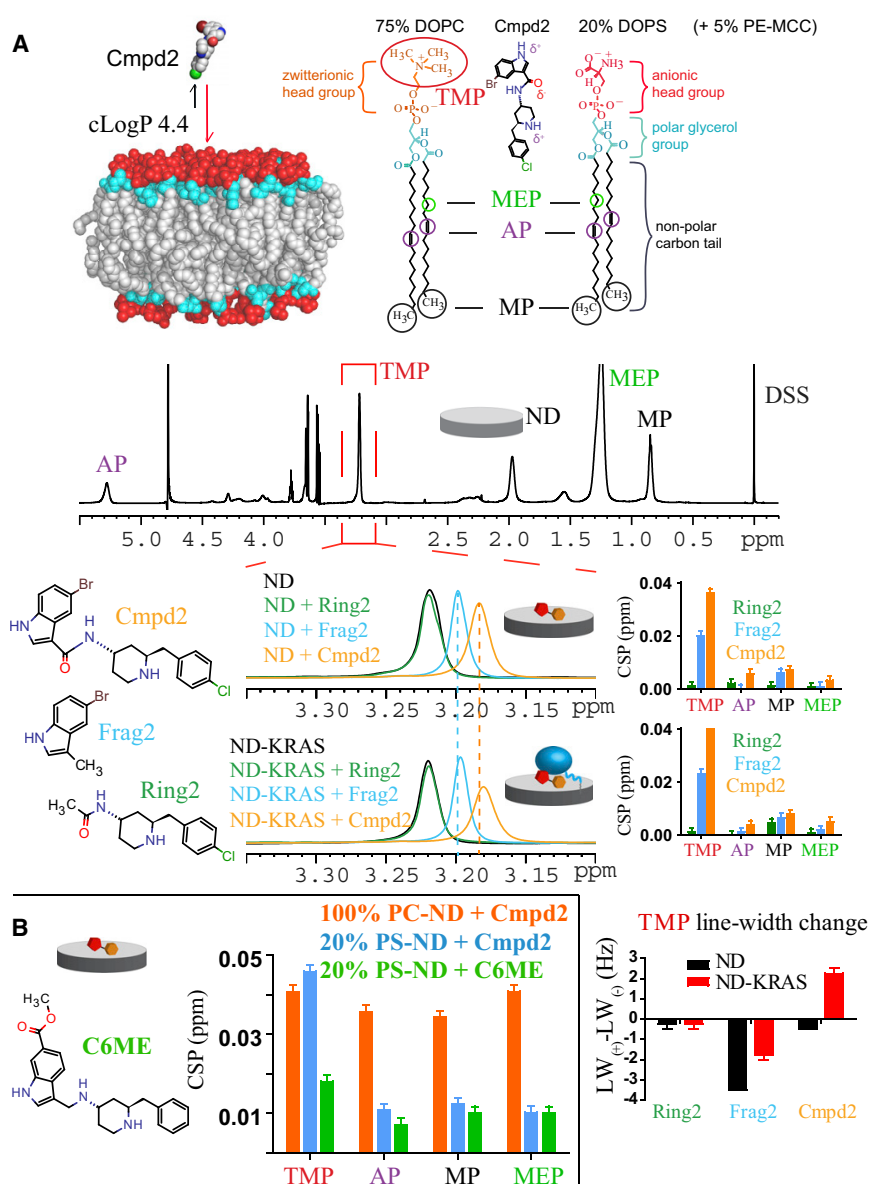
Figure 6. Cmpd2 Inserts into the Lipid Bilayer with the K-RAS4B-Binding Indole Moiety Near the Surface

(A) Cmpd2 (cLogP = 4.4) partitions into the lipid bilayer and perturbs chemical shifts of lipid protons. Compound 2 is shown alongside DOPC and DOPS (head groups, red; glycerol moiety, cyan; hydrocarbon tails, black), and the locations of lipid protons with well-resolved resonances are indicated: methyl protons (MP), alkene protons (AP), methylene protons (MEP), and trimethylamine protons (TMP). Middle: 1D NMR spectrum of DOPC/DOPS nanodiscs, with or without KRAS conjugated, with resonance assignments indicated. Bottom panels: chemical shift perturbation of TMP (left), magnitude of chemical shift changes (right) and TMP line-width changes (bottom) induced by Frag2, Ring2, and Cmpd2 (structures shown at left). Error bars represent the digital resolution of each NMR experiment.

(B) Effect of lipid composition and compound modification on interactions with nanodiscs. Chemical shift perturbation of lipid resonances (80% DOPC/20% DOPS) by Cmpd2 versus C6ME, and effect of lipid composition (100% DOPC versus 80% DOPC/20% DOPS) on Cmpd2-induced perturbations. Error bars represent the digital resolution in the NMR experiment.

See also Figures S4, S5, and S7.

^{1}H resonance (trimethylamine protons [TMP]) of the DOPC head group was perturbed by addition of Cmpd2 or Frag2, but not Ring2 (Figure 6A), suggesting that Cmpd2 effectively associates with the bilayer in a manner in which the indole moiety is at the surface and the Ring2 moiety is more buried in the bilayer (Figure 6A). Further, the presence of K-RAS4B G12V tethered to nanodiscs enhanced the Cmpd2-induced CSP and line broadening of the TMP resonance (Figure 6A), suggesting that binding of K-RAS4B G12V to Cmpd2 may stabilize the complex on the surface of the bilayer.

Since our CSP data suggested an interaction between lipid head groups and Cmpd2, we examined how the lipid composition may affect Cmpd2 interactions with the bilayer. In the absence of DOPS, Cmpd2 induced larger CSPs on the acyl chains (alkene protons [AP], methyl protons [MP], and methylene protons [MEP]) of 100% DOPC nanodiscs (Figure 6B), suggest-

ing that interactions with PS head groups may restrain Cmpd2 at the bilayer surface. C6ME (cLogP: 3.0) induced similar CSPs on the lipid acyl chain protons (MP, AP, and MEP), although it had less effect on the DOPC head group (TMP) relative to Cmpd2 (Figure 6B), indicating that this analog retains interaction with the bilayer and implicating its failure to bind K-RAS for its weak inhibitory effect in the coupled assay. Taken together, these data highlighted the importance of lipid composition and compound structure for maintaining compounds at the bilayer surface.

Structural models of a tripartite complex between Cmpd2-bound K-RAS4B G12V in association with a lipid bilayer were generated by HADDOCK based on the distance restraints derived from PRE data obtained from the membrane-bound state (Table S1, right panel), NOEs between K-RAS4B and Cmpd2 in solution (Table S6), and CSPs induced by the interactions between compounds/fragments and lipids (Figure 6), as described above and summarized in Table S4. When probes exhibiting medium and strong PRE (I*/I^{o} < 0.6, Figure 1) were used as restraints (Figures 4A and S2B), the exposed orientations were predominant in the absence of Cmpd2 (71% of HADDOCK solutions) (Figure 2A), whereas the presence of Cmpd2 increased the population of the occluded cluster substantially from 6.5% to 52% (Figure 4C). To assess the impact of the PRE threshold chosen to define distance restraints in HADDOCK, additional models were generated using higher
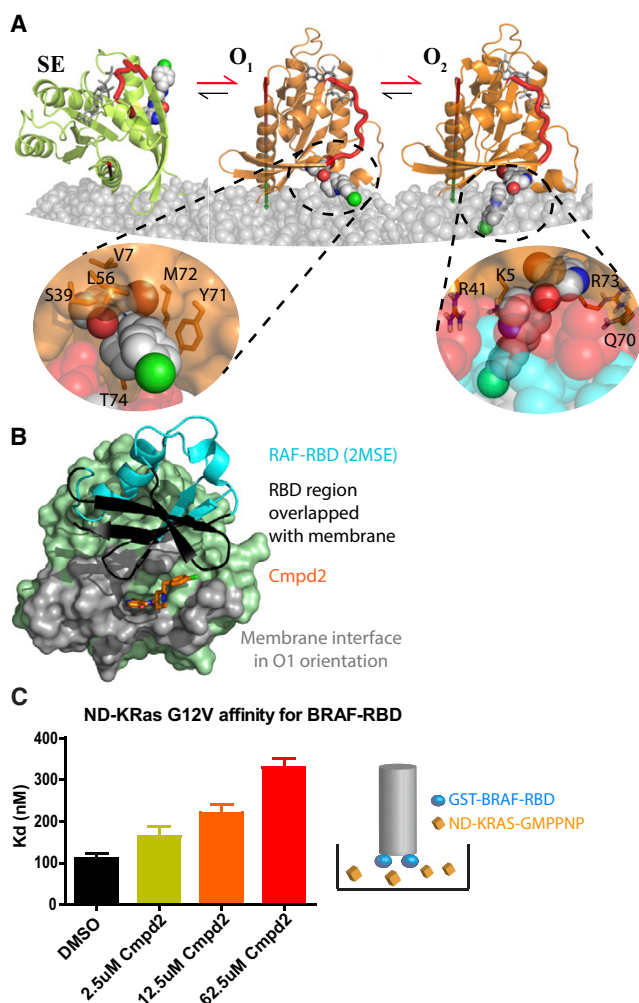
Figure 7. Cmpd2 Stabilizes an Occluded State of K-RAS4B G12V that Is Incompatible with RAF RBD Binding

(A) HADDOCK structural models of nanodisc-tethered K-RAS4B G12V in complex with Cmpd2. In these models, Cmpd2 can bind the exposed or semi-exposed (SE) states, promoting a shift toward the occluded (O_1) orientation. The hydrophobic piperidine-chlorobenzyl rings are then released from K-RAS4B as they insert into the lipid bilayer (O_2). Cmpd2 partitions strongly into the lipid bilayer with the K-RAS4B-binding indole moiety at the surface, which increases its local effective concentration, favoring K-RAS4B binding. Insets: details of Cmpd2 interactions with K-RAS4B and lipids (head groups, red; glycerol moiety, cyan) in O_1 and O_2 orientations.

(B) Mapping Cmpd2, effector protein and membrane binding sites in occluded orientation. Structure of KRAS GTPase domain (green) in complex with ARAF RBD (cyan ribbon) with Cmpd2 (orange) docked. KRAS residues that contact the membrane surface in the O_1 orientation are colored gray and regions of the RBD that would cause steric clashes with the membrane in this orientation are colored black.

(C) Cmpd2 impairs nanodisc-tethered K-RAS4B G12V interaction with BRAF-RBD. K_d values were determined by BLI experiments in which BRAF-RBD was immobilized on the biosensor and nanodisc-tethered K-RAS4B-GMPPNP was in solution with increasing concentrations of Cmpd2. K-RAS4B-GDP was used as a reference and the small non-specific response was subtracted. Error bars represent SD of three independent experiments.

See also Figure S4 and Table S4.

and lower PRE thresholds (I^*/I^o <0.5 or <0.7) (as shown in Figures 1A and 1B). In all cases the HADDOCK models (Figures S6A–S6D) unequivocally exhibit an increase in the population of the occluded orientation induced by Cmpd2. Inspection of the generated models shows that the indole ring of Cmpd2, which is well defined with several NOE restraints to the protein, bridges K-RAS4B G12V and the surface of the bilayer (Figures S4A and 7A). When restraints based on NOEs observed in solution between the piperidine/chlorobenzyl rings and switch $I/\alpha2$ of K-RAS4B are included in the HADDOCK model, these rings further bridge K-RAS4B and the bilayer surface, stabilizing the occluded state (Figure 7A, O_1 orientation). The spatial locations of these rings in this tripartite complex could not be precisely determined due to broadening of their resonances; however, we postulate that they may detach from K-RAS4B switch $I/\alpha2$ and insert into the bilayer driven by interactions between the partially positively charged (δ+) piperidine and the negatively charged lipid phosphate groups, as well as between the hydrophobic chlorobenzyl rings and the glycerol/fatty acid tails, respectively (Figure 6A), thus anchoring the occluded state of K-RAS4B (Figure 7A O_2 orientation). The models further revealed that the K-RAS4B/membrane interface stabilized by Cmpd2 is composed of K5, R41, L52, Q70, and R73 from $\beta1-3$ and $\alpha2$, which further decorate the hydrophobic indole-binding site with positively charged amino acids, all together enhancing the occlusion of the binding site for RBDs by the membrane (Figure 7B).

Cmpd2 Impairs the K-RAS4B Interaction with the RBD of RAF on Bilayers

Notably, there is no direct steric clash between Cmpd2 bound to K-RAS4B and RBDs in isolation without membranes (Figure 7B, PDB: 2MSE). To determine whether Cmpd2 stabilization of the occluded orientation of membrane-anchored K-RAS4B is sufficient to prevent interactions with effector proteins, we performed BLI experiments in which the RBD of BRAF was immobilized on a biosensor, and the binding of nanodisc-tethered K-RAS4B was assessed in the presence of increasing Cmpd2 concentrations. The addition of Cmpd2 lowered the affinity of RBD to K-RAS4B in a dose-dependent manner up to 3-fold at 62 μM (Figure 7C), indicating that it inhibits effector binding when K-RAS4B G12V is bound to membranes. However, Cmpd2 did not impact RBD binding to soluble KRAS, demonstrating that this effect is dependent on the presence of a bilayer. The extent to which Cmpd2 inhibited RBD binding is not sufficient to fully explain its potency in the inhibition of KRAS-mediated activation of full-length RAF kinase activity (IC_{50} < 1 μM). Activation of RAF by RAS is complex, and while the structural details are not fully understood, RAS binding to the RBD disrupts auto-inhibitory interactions between the RBD and cysteine-rich domain (CRD) and the kinase domain. This enables association of the CRD with PS in the membrane and dimerization of the kinase domain, which stabilizes the active conformation of the catalytic site (Lavoie and Therrien, 2015). This sensitive multi-step process can be disrupted by mechanisms other than blocking RAS binding, for example, the monobody "NS1" impairs the ability of RAS to activate RAF by preventing RAS dimerization and nanoclustering (Spencer-Smith et al., 2017). By binding to KRAS and altering its orientation on the membrane, Cmpd2 may interfere with the

RAS-mediated assembly of an active RAF dimer. The mode of Cmpd2 binding defined here provides a foundation for further investigation.

While the aforementioned binding site of Cmpd2 on K-RAS4B coincides with the site previously described for the lead compounds DCAI and Cmpd13 (Maurer et al., 2012; Sun et al., 2012), these compounds were reported to inhibit the activation of RAS by the guanine nucleotide exchange factor (GEF) SOS (Maurer et al., 2012; Sun et al., 2012), rather than interfere with activation of BRAF. The latter may be a more favorable mechanism of action, since oncogenic RAS mutants with impaired GTP hydrolysis and/or rapid intrinsic nucleotide exchange exist in a highly activated, GTP-bound state, even in the absence of GEF activity (Schubbert et al., 2007; Vigil et al., 2010). Our study strongly argues that Cmpd2 acts like a molecular glue between K-RAS4B G12V and the membrane: a tripartite interaction between K-RAS4B G12V, lipid bilayers, and Cmpd2 reduces KRAS binding to effector proteins by stabilizing an orientation in which the effector-binding site is not accessible (Figure 7B). Under conditions in which Cmpd-2 cannot fully prevent RAF from binding to KRAS, Cmpd2 may still hinder the ability of KRAS to promote assembly of an activated RAF dimer. While Cmpd2, like all other non-covalent RAS inhibitors reported to date, has modest affinity for KRAS in solution, its unique mechanism of action enhances its IC_{50} by orders of magnitude when K-RAS4B is associated with a bilayer, which is a requirement for signaling in vivo (Jansen et al., 2017).

While the PRE data clearly demonstrate that the K-RAS4B conformational state on a lipid bilayer markedly shifts toward the auto-inhibited occluded state (O_2 in Figure 7A), K-RAS4B remains in dynamic equilibrium with other states including the SE and exposed states (E_1-E_3). This is consistent with the effective rotational correlation time (τ_c) measurements (Lee et al., 2006) of ^{15}N-labeled K-RAS4B (Figures S7A and S7B), which indicates that addition of Cmpd2 resulted in only a marginal increase in the τ_c value (40.5 ns in the presence of Cmpd2 versus 39.6 ns in the absence of Cmpd2). Free K-RAS4B and K-RAS4B rigidly associated with the >100-kDa nanodisc complex would have predicted τ_c values of <20 and >60 ns, respectively, thus the intermediate τ_c value (39.6 ns) of K-RAS4B tethered to nanodiscs indicates that the K-RAS4B GTPase domain interaction with membrane is very dynamic. The marginal increase in the τ_c value by Cmpd2 indicates that this interaction remains transient and dynamic in the presence of Cmpd2. Compared to free K-RAS4B, the addition of Cmpd2 to GMPPNP-bound K-RAS4B G12V (1–185) on nanodiscs induced substantial peak broadening and minor CSPs (Figures S7C and S7D). We speculate that the population of K-RAS4B transiently bound to Cmpd2 at the surface of the nanodisc may be undetectable because of its reduced rate of tumbling and an intermediate to fast rate of exchange with other states of KRAS on the bilayer. It is remarkable to note that, even in such a dynamic system, PRE is extremely sensitive to changes in protein conformational equilibrium, providing valuable insights into the mechanism for the enhanced efficacy of Cmpd2 against the membrane-associated form of K-RAS4B. On the other hand, because the PRE effect becomes insignificant beyond 25 Å (Gottstein et al., 2012), conformers that are not in proximity to the membrane

are not observable by PRE, thus other methods are needed to characterize these species.

The potent IC_{50} of Cmpd2 observed in cell-based assays may involve enrichment of Cmpd2 on the bilayer surface, which would increase its local concentration and drive saturation of K-RAS. Partitioning into the membrane is proposed to be important for many drugs that target membrane-associated proteins (Mayne et al., 2016), including general anesthetics, which bind with low affinity to a lipid bilayer-accessible cavity of pentameric ligand-gated ion channels (Nury et al., 2011). A better understanding of this complex will set the stage for optimizing the structure-activity relationship of Cmpd2 as well as development of novel compounds that exploit targeting the RAS/membrane interface for effective RAS inhibition. The NMR-based approach presented here offers a unique conformational assay for inhibitor screening, which is extremely sensitive to small molecules that can target the molecular interface between K-RAS4B and lipid bilayers.

SIGNIFICANCE

The *KRAS* gene is frequently mutated in human cancers, including most pancreatic, one in three colon, and one in six lung tumors, which represent three of the five leading causes of cancer deaths worldwide. Mutant KRAS has long been recognized as a driver of oncogenic processes in these cells; however, the hyper-activated mutant protein is a challenging target, due to a lack of classical "druggable" pockets. Aside from covalent inhibitors of an infrequent G12C mutant, all reported lead compounds suffer from low affinity, and no KRAS inhibitors have progressed to the clinic. Because KRAS oncogenic signaling requires prenylation and association with the cellular membrane, we postulated that the KRAS:membrane interface would be an attractive target for drug discovery. In this study, we revealed a unique mechanism of action by which the small molecule Cmpd2 blocks K-RAS4B signaling by simultaneously engaging both a shallow pocket on K-RAS4B and the lipid bilayer. Cmpd2 thereby stabilizes K-RAS4B in an orientation on the membrane in which its effector-binding site is occluded, which impairs interaction with and activation of RAF kinase. Further, partitioning of Cmpd2 onto the bilayer surface may promote binding to KRAS, and contribute to enhancing its IC_{50} by orders of magnitude for K-RAS4B in the presence of membranes, relative to its modest affinity for KRAS in solution. This approach of targeting a protein-membrane interface for inhibitor development sets the stage for exploiting this mechanism of action for development of novel inhibitors of KRAS, other RAS isoforms and related small GTPases, as well as other membrane-associated proteins.

STAR★METHODS

Detailed methods are provided in the online version of this paper and include the following:

- KEY RESOURCES TABLE
- CONTACT FOR REAGENT AND RESOURCE SHARING

AUTHOR CONTRIBUTIONS

Z.F., C.B.M., J.M.J., W.J., and M.I. conceived the project, and Z.F., C.B.M., and M.I. designed the experiments. Z.F. conducted most of the experiments, A.D.G. collected and analyzed NOE data and W.J. collected C6ME CSP data. J.M.J. and W.J. contributed new reagents. Z.F., C.B.M., T.N., A.D.G., J.M.J., W.J., and M.I. analyzed the results. Z.F., C.B.M., and M.I. wrote the paper.

DECLARATION OF INTERESTS

Z.F., C.B.M., T.N., and M.I. declare no competing financial interests. A.D.G., J.M.J., and W.J. were employees of Novartis Institutes for BioMedical Research at the time of these studies and may own stock in the company. This does not alter our adherence to journal policies on sharing data and materials. None of the authors have competing interests relating to employment, consultancy, patents, products in development, or marketed products.

REFERENCES

Breeze, A.L. (2000). Isotope-filtered NMR methods for the study of biomolecular structure and interactions. Prog. Nucl. Magn. Reson. Spectrosc. 36, 323–372.

Cox, A.D., Fesik, S.W., Kimmelman, A.C., Luo, J., and Der, C.J. (2014). Drugging the undruggable RAS: mission possible? Nat. Rev. Drug Discov. 13, 828–851.

Delaglio, F., Grzesiek, S., Vuister, G.W., Zhu, G., Pfeifer, J., and Bax, A. (1995). NMRPipe: a multidimensional spectral processing system based on UNIX pipes. J. Biomol. NMR 6, 277–293.

Denisov, I.G., Grinkova, Y.V., Lazarides, A.A., and Sligar, S.G. (2004). Directed self-assembly of monodisperse phospholipid bilayer nanodiscs with controlled size. J. Am. Chem. Soc. 126, 3477–3487.

Gossert, A.D., Hiller, S., and Fernandez, C. (2011). Automated NMR resonance assignment of large proteins for protein-ligand interaction studies. J. Am. Chem. Soc. 133, 210–213.

Goto, N.K., Gardner, K.H., Mueller, G.A., Willis, R.C., and Kay, L.E. (1999). A robust and cost-effective method for the production of Val, Leu, Ile (delta 1) methyl-protonated 15N-, 13C-, 2H-labeled proteins. J. Biomol. NMR 13, 369–374.

Gottstein, D., Reckel, S., Dotsch, V., and Guntert, P. (2012). Requirements on paramagnetic relaxation enhancement data for membrane protein structure determination by NMR. Structure 20, 1019–1027.

Hunter, J.C., Manandhar, A., Carrasco, M.A., Gurbani, D., Gondi, S., and Westover, K.D. (2015). Biochemical and structural analysis of common cancer-associated KRAS mutations. Mol. Can Res. 13, 1325–1335.

Jansen, J.M., Wartchow, C., Jahnke, W., Fong, S., Tsang, T., Pfister, K., Zavorotinskaya, T., Bussiere, D., Cheng, J.M., Crawford, K., et al. (2017). Inhibition of prenylated KRAS in a lipid environment. PLoS One 12, e0174706.

Kobashigawa, Y., Harada, K., Yoshida, N., Ogura, K., and Inagaki, F. (2011). Phosphoinositide-incorporated lipid-protein nanodiscs: a tool for studying protein-lipid interactions. Anal Biochem. 410, 77–83.

Lee, D., Hilty, C., Wider, G., and Wuthrich, K. (2006). Effective rotational correlation times of proteins from NMR relaxation interference. J. Magn. Reson. 178, 72–76.

Lavoie, H., and Therrien, M. (2015). Regulation of RAF protein kinases in ERK signalling. Nat. Rev. Mol. Cell Biol. 16, 281–298.

Lee, W., Tonelli, M., and Markley, J.L. (2015). NMRFAM-SPARKY: enhanced software for biomolecular NMR spectroscopy. Bioinformatics 31, 1325–1327.

Maurer, T., Garrenton, L.S., Oh, A., Pitts, K., Anderson, D.J., Skelton, N.J., Fauber, B.P., Pan, B., Malek, S., Stokoe, D., et al. (2012). Small-molecule ligands bind to a distinct pocket in Ras and inhibit SOS-mediated nucleotide exchange activity. Proc. Nat. Acad. Sci. USA 109, 5299–5304.

Mayne, C.G., Arcario, M.J., Mahinthichaichan, P., Baylon, J.L., Vermaas, J.V., Navidpour, L., Wen, P.C., Thangapandian, S., and Tajkhorshid, E. (2016). The cellular membrane as a mediator for small molecule interaction with membrane proteins. Biochim. Biophys. Acta 1858, 2290–2304.

Mazhab-Jafari, M.T., Marshall, C.B., Smith, M.J., Gasmi-Seabrook, G.M., Stathopulos, P.B., Inagaki, F., Kay, L.E., Neel, B.G., and Ikura, M. (2015). Oncogenic and RASopathy-associated K-RAS mutations relieve membrane-dependent occlusion of the effector-binding site. Proc. Nat. Acad. Sci. USA 112, 6625–6630.

Muraoka, S., Shima, F., Araki, M., Inoue, T., Yoshimoto, A., Ijiri, Y., Seki, N., Tamura, A., Kumasaka, T., Yamamoto, M., et al. (2012). Crystal structures of the state 1 conformations of the GTP-bound H-Ras protein and its oncogenic G12V and Q61L mutants. FEBS Lett. 586, 1715–1718.

Nury, H., Van Renterghem, C., Weng, Y., Tran, A., Baaden, M., Dufresne, V., Changeux, J.P., Sonner, J.M., Delarue, M., and Corringer, P.J. (2011). X-Ray structures of general anaesthetics bound to a pentameric ligand-gated ion channel. Nature 469, 428–431.

Ostrem, J.M., and Shokat, K.M. (2016). Direct small-molecule inhibitors of KRAS: from structural insights to mechanism-based design. Nat. Rev. Drug Discov. 15, 771–785.

Prakash, P., Zhou, Y., Liang, H., Hancock, J.F., and Gorfe, A.A. (2016). Oncogenic K-Ras binds to an anionic membrane in two distinct orientations: a molecular dynamics analysis. Biophys. J. 110, 1125–1138.

Prior, I.A., Lewis, P.D., and Mattos, C. (2012). A comprehensive survey of Ras mutations in cancer. Cancer Res. 72, 2457–2467.

Schubert, S., Shannon, K., and Bollag, G. (2007). Hyperactive Ras in developmental disorders and cancer. Nat. Rev. Cancer 7, 295–308.

Schuler, M.A., Denisov, I.G., and Sligar, S.G. (2013). Nanodiscs as a new tool to examine lipid-protein interactions. Methods Mol. Biol. *974*, 415–433.

Schuttelkopf, A.W., and van Aalten, D.M. (2004). PRODRG: a tool for high-throughput crystallography of protein-ligand complexes. Acta Crystallogr. D Biol. Crystallogr. *60*, 1355–1363.

Smith, M.J., and Ikura, M. (2014). Integrated RAS signaling defined by parallel NMR detection of effectors and regulators. Nat. Chem. Biol. *10*, 223–230.

Spencer-Smith, R., Koide, A., Zhou, Y., Eguchi, R.R., Sha, F., Gajwani, P., Santana, D., Gupta, A., Jacobs, M., Herrero-Garcia, E., et al. (2017). Inhibition of RAS function through targeting an allosteric regulatory site. Nat. Chem. Biol. *13*, 62–68.

Spiegel, J., Cromm, P.M., Zimmermann, G., Grossmann, T.N., and Waldmann, H. (2014). Small-molecule modulation of Ras signaling. Nat. Chem. Biol. *10*, 613–622.

Stephen, A.G., Esposito, D., Bagni, R.K., and McCormick, F. (2014). Dragging ras back in the ring. Cancer Cell *25*, 272–281.

Sun, Q., Burke, J.P., Phan, J., Burns, M.C., Olejniczak, E.T., Waterson, A.G., Lee, T., Rossanese, O.W., and Fesik, S.W. (2012). Discovery of small molecules that bind to K-Ras and inhibit Sos-mediated activation. Angew. Chem. Int. Ed. *51*, 6140–6143.

van Zundert, G.C., Rodrigues, J.P., Trellet, M., Schmitz, C., Kastritis, P.L., Karaca, E., Melquiond, A.S., van Dijk, M., de Vries, S.J., and Bonvin, A.M. (2016). The HADDOCK2.2 web server: user-friendly integrative modeling of biomolecular complexes. J. Mol. Biol. *428*, 720–725.

Vigil, D., Cherfils, J., Rossman, K.L., and Der, C.J. (2010). Ras superfamily GEFs and GAPs: validated and tractable targets for cancer therapy? Nat. Rev. Cancer *10*, 842–857.

Zwahlen, C., Legault, P., Vincent, S.J.F., Greenblatt, J., Konrat, R., and Kay, L.E. (1997). Methods for measurement of intermolecular NOEs by multinuclear NMR spectroscopy: application to a bacteriophage λ N-peptide/boxB RNA complex. J. Am. Chem. Soc. *119*, 6711–6721.

STAR★METHODS

KEY RESOURCES TABLE

REAGENT or RESOURCE	SOURCE	IDENTIFIER
Antibodies		
Rabbit polyclonal anti-phospho-MEK1/2 antibody	Cell Signaling	#9121, RRID: AB_331648
Bacterial and Virus Strains		
BL21 Codon Plus (DE3)	Thermo Fisher	Cat. No. NC9122855
Chemicals, Peptides, and Recombinant Proteins		
methyl-13C; 3,3-D2 α-ketobutyrate	Cambridge Isotope Laboratories	CDLM-7318
3-methyl-13C; 3,4,4,4-D4 α-ketoisovalerate	Cambridge Isotope Laboratories	CDLM-7317
1,2-dioleoyl-sn-glycero-3-phosphocholine (DOPC)	Avanti Polar Lipids	#850375c
1,2-dioleoyl-sn-glycero-3-phospho-L-serine (DOPS)	Avanti Polar Lipids	#840035c
1,2-dioleoyl-sn-glycero-3-phosphoethanolamine-N-[4-(p-maleimidomethyl) cyclohexane-carboxamide] (PE-MCC)	Avanti Polar Lipids	#780201c
1,2-distearoyl-sn-glycero-3-phosphoethanolamine-N diethylenetriaminepentaacetic acid, PE-DTPA (Gd3+)	Avanti Polar Lipids	#791275
Tris(2-carboxyethyl) phosphine hydrochloride (TCEP)	Bioshop	TCE101.10
Guanosine 5′-[β,γ-imido]triphosphate trisodium salt hydrate (GMPPNP)	Sigma	G0635
Guanosine 5′-diphosphate sodium salt (GDP)	Sigma	G7127
Guanosine 5′-[γ-thio]triphosphate tetralithium salt (GTPγS)	Sigma	G8634
Cmpd2	Jansen et al., 2017	N/A
Frag2	Sigma	752355
Ring2	This paper	N/A
C6ME	This paper	N/A
Isopropyl-1-thio-β-D-galacto-pyranoside (IPTG)	Bioshop	IPT001
Thrombin (bovine)	BioPharm	91-035
Calf intestinal alkaline phosphatase (CIP)	NEB	M0290
Bio-beads SM-2	Bio-Rad	1528920
Superdex-200	GE Life Sciences	17104301
Critical Commercial Assays		
AlphaScreen with anti-phospho-MEK antibody	PerkinElmer	#6760671
Bio-Layer Interferometry (BLI) assay, Anti-GST biosensor	ForteBio	Octet RED384 18-5096
Deposited Data		
Structure of Nanodisc-tethered K-RAS4B-GMPPNP (E3 state)	This paper	PDB: 6CCH
Structure of Nanodisc-tethered K-RAS4B-GMPPNP in complex with Cmpd2 (O1 state)	This paper	PDB: 6CC9
Structure of Nanodisc-tethered K-RAS4B-GMPPNP in complex with Cmpd2 (O2 state)	This paper	PDB: 6CCX
Recombinant DNA		
Plasmid: pET28a KRAS4B (1-185, C118S)	Mazhab-Jafari et al., 2015	N/A
Plasmid: pET28a KRAS4B (1-185, C118S) G12V	This paper	N/A
Plasmid: pGBHPS-MSP	Kobashigawa et al., 2011	N/A
Plasmid: pGEX4T2 BRAF RBD (150-233)	Smith and Ikura, 2014	N/A

(Continued on next page)

CONTACT FOR REAGENT AND RESOURCE SHARING

Further information and requests for resources and reagents should be directed to and will be fulfilled by the Lead Contact, Mitsu Ikura (mikura@uhnresearch.ca). Plasmids require a material transfer agreement from the University Health Network Technology Development and Commercialization Office. Compounds require a material transfer agreement from Novartis Institutes for BioMedical Research.

EXPERIMENTAL MODEL AND SUBJECT DETAIL

Bacterial Strain and Culture Conditions

Expression of proteins used for biophysical studies and assays was performed in E. coli BL21 codon plus (DE3). Cells were grown at 37°C in Luria-Bertani (LB) broth. When optical density at 600 nm reached 0.6–0.7, protein expression was induced with the addition of 0.5 mM IPTG and cells were incubated for 16–18 h at 15°C before harvest.

METHOD DETAILS

Protein Preparation

Human K-RAS4B (residues 1-185, bearing a C118S mutation) and the G12V, G12V T74W mutant were expressed as His-tagged proteins in Escherichia coli (BL21 DE3 Codon+) from the pET28a vector as described previously (Mazhab-Jafari et al., 2015). BRAF RBD (residues 150-233) was expressed as a GST fusion from pGEX4T2 as described by Smith and Ikura (2014). Bacteria were grown either in lysogeny broth (LB) or minimal M9 media supplemented with $^{15}NH_4Cl$ or methyl-^{13}C; 3,3-D2 α-ketobutyrate (CIL, CDLM-7318) and 3-methyl-^{13}C; 3,4,4,4-D4 α-ketoisovalerate (CIL, CDLM-7317) to label amides or Ile, Leu and Val methyl groups, respectively. Protein expression was induced with 0.25 mM isopropyl-1-thio-β-D-galacto-pyranoside (IPTG) at 15°C overnight. Proteins were purified using Ni-NTA or Glutathione Sepharose resin, and His tags were removed by thrombin. The thrombin-cleaved proteins were further purified by size exclusion chromatography using a Superdex-75 column (GE Healthcare). Purified K-RAS4B was then loaded with GMPPNP in the presence of EDTA and Calf intestinal alkaline phosphatase (CIP), which were removed along with the excess nucleotide by passage through a Superdex-75 column (GE Healthcare). Membrane scaffold protein 1D1 (MSP1D1) was prepared as described previously (Kobashigawa et al., 2011; Mazhab-Jafari et al., 2015).

Preparation of Nanodisc-Tethered K-RAS4B

All lipids were purchased from Avanti Polar Lipids and were mixed in chloroform solutions, then air-dried with nitrogen flow and re-solubilized with cholate in aqueous buffer (20mM HEPES pH 7.4, 100mM NaCl and 100mM sodium cholate). Nanodiscs were prepared using 1,2-dioleoyl-sn-glycero-3-phosphocholine (DOPC), 1,2-dioleoyl-sn-glycero-3-phospho-L-serine (DOPS), and the thiol-reactive lipid 1,2-dioleoyl-sn-glycero-3-phosphoethanolamine-N-[4-(p-maleimidomethyl) cyclohexane-carboxamide] (PE-MCC) in a molar ratio of 15:4:1. For PRE experiments, 1,2-distearoyl-sn-glycero-3-phosphoethanolamine-N diethylenetriamine-pentaacetic acid [gadolinium salt; PE-DTPA (Gd^{3+})] was added to the lipid mixture to a final molar ratio of 2.5% of the total lipids. Nanodiscs were assembled by mixing MSP1D1 with solubilized lipids at a 1:40 ratio followed by removal of sodium cholate from the mixture with Bio-beads SM-2 (Bio-Rad). Assembled nanodiscs were then purified via a Superdex-200 size exclusion column (GE Healthcare). K-RAS4B was then covalently linked to PE-MCC in preassembled, purified nanodiscs as described previously (Mazhab-Jafari et al., 2015), and this complex was purified on a Superdex-200 column. The average number of K-RAS4B molecules tethered to the nanodiscs was estimated based on the ratio of K-RAS4B to MSP1D1 in SDS-PAGE.

NMR Spectroscopy

NMR data were acquired at 25°C on 600 and 800 MHz Bruker AVANCE II spectrometers equipped with 5 mm TCI CryoProbes. Protein samples were prepared in a sample buffer containing 20 mM HEPES (pH 7.4), 100 mM NaCl, 5 mM MgCl2, 2 mM Tris(2-carboxyethyl) phosphine hydrochloride (TCEP) at protein concentrations of 0.2 mM. Cmpd2 was added to nanodisc-tethered K-RAS4B at a ratio of

5:1 in CSP experiments, PRE experiments and one-dimensional proton NMR experiments. ^{1}H-^{13}C Heteronuclear multiple quantum correlation (HMQC) and ^{1}H-^{15}N transverse relaxation optimized spectroscopy (TROSY) spectra were collected with 16 and 64 scans, respectively, for nanodisc-tethered K-RAS4B and nanodisc-tethered K-RAS4B:Cmpd2 complexes. ^{1}H-^{15}N heteronuclear single quantum coherence (HSQC) spectra with 8 scans and one-dimensional proton NMR spectra with 128 scans were used for chemical shift perturbation experiments. Protein-ligand intermolecular NOEs were obtained from NOESY spectra collected from a 0.4 mM sample of GDP-bound KRAS (1-169) in presence of 1 mM Cmpd2, using assignments from (Gossert et al., 2011). 2D F1-edited, F2-filtered double-half filter experiments were used with a mixing time of 200 ms and 24 h of recording time (Breeze, 2000; Zwahlen et al., 1997). Additional ligand-protein NOEs were extracted from the ligand plane of an all-in-one NOESY experiment with 120 ms mixing time recorded in 60 h. In order to resolve ambiguities in NOE assignments, a high-resolution spectrum was recorded on a specifically ILVM ^{13}C-methyl labeled sample (Goto et al., 1999). K-RAS4B isoleucine-Cδ methyls were assigned in our previous study (Mazhab-Jafari et al., 2015), and valine-Cγ and leucine-Cδ methyl resonances were assigned based on the assignment of T35S H-RAS-GMPPNP [Biological Magnetic Resonance Bank (BMRB) code 17610]. K-RAS4B backbone amide assignments were transferred from K-RAS-GMPPNP [BMRB code 17785]. NMR spectra were processed with NMRPipe(Delaglio et al., 1995) (www.ibbr.umd.edu/nmrpipe) and analyzed with Sparky (Lee et al., 2015)(https://www.cgl.ucsf.edu/home/sparky/). For PRE measurements, the intensities of resonances from K-RAS4B attached to PE-DTPA (Gd^{3+})-containing nanodiscs (I*) and those of a control sample lacking PE-DTPA (Gd^{3+}) (I^o) were measured by Gaussian line fitting, and the ratio (I*/I^o) was calculated. Small differences in the concentrations of PRE and control samples were corrected by normalization of the calculated intensity ratios using the highest 5% observed I*/I^o values.

Measurement of Rotational Correlation Time

The [^{15}N, ^{1}H]-TRACT pulse sequence (Lee et al., 2006) was used to determine rotational correlation time (τ_c) of nanodisc-tethered ^{15}N KRAS-GMPPNP at a concentration of 0.2 mM, with or without addition of 1 mM Cmpd2. Relaxation data were recorded on an 800 MHz Bruker spectrometer with variable relaxation delays (2, 4, 8, 12, 16, 24, 32, 40, 48, 64, 80, 96, 112, 128, 144, and 176 ms). The τ_c value was calculated with the parameters $\theta=17°$, $r_{HN}=1.02$ Å and $\Delta\delta_N= 160$ ppm as described by (Lee et al., 2006). The τ_c was calculated from the difference of the relaxation rates of the α and β states (R$_\alpha$ and R$_\beta$), which were derived from fitting the integrals of amide protons between 8.2 and 9.5 ppm to single exponential decay curves. The 8.2-9.5 ppm spectral region was chosen to select amide proton resonances from structured regions and reduce the impact of flexible residues on measured τ_c. The calculated τ_c represents the lower limit of τ_c due to a rigid body assumption.

BLI Assays

Bio-Layer Interferometry (BLI) assays were performed using an Octet RED384 instrument (ForteBio) to measure the affinity of interactions between BRAF-RBD and nanodisc-tethered K-RAS4B. A GST fusion protein of BRAF-RBD (GST-BRAF-RBD) was immobilized on biosensors coated with an antibody recognizing GST and the association of nanodisc-conjugated K-RAS4B-GMPPNP was measured at 25 degrees across a range of K-RAS4B concentrations (250, 125, 62.5, 31.3, 15.6, and 7.8 nM) for 400s in buffer comprising 20 mM HEPES (pH 7.4), 100 mM NaCl, 5 mM MgCl$_2$, 2 mM TCEP. The concentration of nanodisc-tethered K-RAS4B was estimated based on the total protein concentration of the sample measured by Bradford and an estimated K-RAS4B:MSP ratio of 1:2. Nanodisc-tethered K-RAS4B-GDP exhibited minimal binding and served as a reference sample to subtract non-specific binding. Dissociation was monitored for 700s after transferring biosensors to sample buffer. The Kd values were calculated from the concentration-dependent steady-state response curve.

Coupled Assay

The assay measuring inhibition of the K-RAS4B-mediated activation of BRAF was performed as described in (Jansen et al., 2017). In brief, prenylated K-RAS4B-GTPγS (2 nM), biotinylated MEK (20 nM), ATP (10 uM) and full-length WT BRAF were combined with PS liposomes (2 ug/ml). Reactions were stopped with 20mM EDTA and 0.003% Tween. AlphaScreen technology (PerkinElmer #6760671) with an anti-phospho-MEK antibody (Cell Signaling #9121) was used to detect phosphorylation of MEK, which was used as readout of BRAF activation. After an overnight incubation, samples were read for emission at 570 nm upon excitation of the donor beads at 680 nm on an Envision 2101 instrument (PerkinElmer).

NOE-, CSP- and PRE- Guided Docking Simulation

All docking simulations were performed using High Ambiguity Driven biomolecular DOCKing (HADDOCK, version 2.2) software (van Zundert et al., 2016).The starting structure of full-length K-RAS4B GMPPNP was derived from PDB: 4DST as previously described (Mazhab-Jafari et al., 2015). The complex formed by K-RAS4B and Cmpd2 in solution was modeled in HADDOCK using restraints derived from intermolecular NOEs (Table S6) and the small ligand docking protocols described in the HADDOCK2.2 manual. A distance range of 1-4 Å was applied to all NOE-based distance restraints in HADDOCK. Due to the lack of protons in the HADDOCK-derived structural model of K-RAS, the proton-proton NOEs were converted to distance restraints between the adjacent carbon atoms of K-RAS4B and protons of the compound. The well-resolved NOEs involving surface-exposed KRAS residues were classified as unambiguous restraints in HADDOCK (Table S6). In addition, on the basis of crystal structures of similar indole moieties of Cmpd13 and DCAI docked to the switch I pocket, NOEs between the indole protons (H2, H3, H6 and H8) and the surface-exposed atoms of the pocket residues (V7, L56 and T74) were made unambiguous. NOEs derived from Cmpd2 peaks that overlap were

translated into ambiguous restraints that could involve either of the overlapping protons, (i.e., H2 or H3; H21 or H25; and H15 or H18). The assignments of H6 and H8 could not be distinguished with certainty, thus NOEs involving these protons were also treated as ambiguous restraints that could involve either proton (i.e., H6 or H8), however both are located within the indole. Overlapping NOEs involving H2 and H3 in the indole and H21 and H25 in the chloro-benzyl ring were resolved by taking into account the consistencies with localization of the indole to the switch I pocket, which is supported by several NOEs involving H6/H8, as well as the crystal structures described above. MarvinSketch software and PRODRG server (Schuttelkopf and van Aalten, 2004) were used to generate 2D and 3D structures of Cmpd2, respectively. The docking protocol comprised a 3,000 rigid-body docking stage and the top 200 HADDOCK scored structures were further refined using semi-flexible simulated annealing, followed by water refinement.

For the model of K-RAS4B in complex with the nanodisc, distance restraints were generated between K-RAS4B atoms sensitive to the PRE effect of PE-DTPA (Gd^{3+}) and any lipid head group atom on the nanodisc surface. The K-RAS4B probes exhibiting PRE-induced broadening beyond established thresholds were defined as PRE-sensitive probes (Table S1, left panel). Three different PRE thresholds were chosen to assess the impact of the threshold value on the resulting HADDOCK models. The PRE-sensitive probes were defined as 'active' residues in HADDOCK, and the adjacent N- and C-terminal residues were defined as 'passive' residues. Ambiguous distance restraints between PRE-sensitive probes and lipid head groups were assigned a range of 2-5 Å, except a range of 0-2 Å was assigned for K-RAS4B C185 to reflect its covalent linkage to PE-MCC. Cluster analysis of HADDOCK models was performed as previously described (Mazhab-Jafari et al., 2015), with an RMSD cutoff of 5 Å and a minimum cluster population of 4. Clusters that exhibit similar orientations were combined. The HADDOCK scores of all 200 structures were plotted against RMSD relative to the mean structure of the 'exposed' orientation cluster.

Models of Cmpd2 docked to nanodisc-tethered K-RAS4B were generated in two steps, whereby Cmpd2-bound K-RAS4B was docked on the nanodisc surface, followed by partial insertion of Cmpd2 into the lipid bilayer. First, two-body docking simulations were performed using NOE-derived models of the K-RAS4B:Cmpd2 complex and the nanodisc to model Cmpd2-bound K-RAS4B interaction with the nanodisc surface based on PRE-based distance restraints listed in Table S1 (right panel). Then this was refined based on 1-D NMR observations of Cmpd2 and its derivative compounds that indicate Cmpd2 partitions into the lipid bilayer with the indole near the choline headgroups and the piperidine-chlorobenzyl rings inserted more deeply (Figures 6 and S5). Initially, three-body (K-RAS4B, Cmpd2 and nanodisc) docking simulations were performed in which the restraints between the piperidine-chlorobenzyl rings of Cmpd2 and K-RAS4B based on NOEs observed in solution (i.e., in the absence of nanodiscs) were removed such that K-RAS4B-bound Cmpd2 was not restricted from inserting into the bilayer. As a result, these rings were predicted to spontaneously insert into the bilayer in ~20% of the HADDOCK solutions. To further develop this 'inserted' model, three-body docking simulations were repeated with the addition of CSP-based ambiguous restraints between the indole ring of Cmpd2 and the choline/serine moieties of the lipid head groups, along with restraints between the piperidine-chlorobenzyl rings and the lipid tails or glycerol moiety, inferred on the basis of severe broadening of the ring proton resonances by nanodiscs (Figure S5).

Compound Information
Synthesis of Cmpd2, 5-bromo-N-((2R,4S)-2-(4-chlorobenzyl)piperidin-4-yl)-1H-indole-3-carboxamide, is described in (Jansen et al., 2017); Synthesis of C6ME, methyl 3-((((2S,4R)-2-benzylpiperidin-4-yl)amino)methyl)-1H-indole-6-carboxylate, was similar to that of compound **3** from (Jansen et al., 2017). Synthesis of Ring2, N-((2R,4S)-2-(4-chlorobenzyl)piperidin-4-yl)acetamide, is described on page 41 (part C) of WO 96/10562. Frag 2, 5-bromo-3-methyl-1H-indole, is commercially available (CAS Registry Number 10075-48-6). The cLogP values of compounds were calculated from ALOGPS 2.1 (http://www.vcclab.org/lab/alogps/).

QUANTIFICATION AND STATISTICAL ANALYSIS

Bar graphs display mean ± standard deviation. Statistical methods were not utilized in analysis of the significance of data in this study.

DATA AND SOFTWARE AVAILABILITY

The coordinates, chemical shifts and distance restraints for the structures of nanodisc-tethered K-RAS4B without Cmpd2 (E3 state) and with Cmpd2 (O1 and O2 states) reported in this paper have been deposited in the PDB under the accession numbers PDB: 6CCH, 6CC9, and 6CCX respectively.